Katabatic flow along a differentially cooled sloping surface

By ALAN SHAPIRO AND EVGENI FEDOROVICH

School of Meteorology, University of Oklahoma, Norman, OK 73072, USA

Buoyancy inhomogeneities on sloping surfaces arise in numerous situations, for example, from variations in snow/ice cover, cloud cover, topographic shading, soil moisture, vegetation type, and land use. In this paper, the classical Prandtl model for one-dimensional flow of a viscous stably stratified fluid along a uniformly cooled sloping planar surface is extended to include the simplest type of surface inhomogeneity – a surface buoyancy that varies linearly down the slope. The inhomogeneity gives rise to acceleration, vertical motions associated with low-level convergence, and horizontal and vertical advection of perturbation buoyancy. Such processes are not accounted for in the classical Prandtl model. A similarity hypothesis appropriate for this inhomogeneous flow removes the along-slope dependence from the problem, and, in the steady state, reduces the Boussinesq equations of motion and thermodynamic energy to a set of coupled nonlinear ordinary differential equations. Asymptotic solutions for the velocity and buoyancy variables in the steady state, valid for large values of the slope-normal coordinate, are obtained for a Prandtl number of unity for pure katabatic flow with no ambient wind or externally imposed pressure gradient. The undetermined parameters in these solutions are adjusted to conform to lower boundary conditions of no-slip, impermeability and specified buoyancy. These solutions yield formulae for the boundary-layer thickness and slope-normal velocity component at the top of the boundary layer, and provide an upper bound of the along-slope surface-buoyancy gradient beyond which steady-state solutions do not exist. Although strictly valid for flow above the boundary layer, the steady asymptotic solutions are found to be in very good agreement with the terminal state of the numerical solution of an initial-value problem (suddenly applied surface buoyancy) throughout the flow domain. The numerical results also show that solution non-existence is associated with self-excitation of growing low-frequency gravity waves.

1. Introduction

In this paper, we extend the one-dimensional Prandtl model (1942) for katabatic/anabatic flow in a stably stratified fluid to include one of the simplest representations of surface inhomogeneity – a surface buoyancy that varies linearly with distance down the slope. Inhomogeneous surface buoyancy fields are ubiquitous in nature. They arise from irregular snow/ice/soil cover, cloud cover, topographic shading (e.g. upper slopes are shaded while lower slopes are sunlit), soil moisture (e.g. from a surface rainfall gradient), variations in vegetation type or coverage, and changes in land use. A down-slope variation in buoyancy also occurs over melting glaciers, where the maintenance of a uniform $0\,^\circ\text{C}$ temperature along the melting surface is associated with a potential temperature decrease down the slope (a decrease that

typically exceeds that associated with the environmental lapse rate). Our extended model is based on a spatial similarity constraint and applies to regions where the surface buoyancy varies slowly enough in the along-slope direction that it is described well locally by a linear variation. It may also apply to a transition zone, with slowly varying buoyancy, bridging two regions of different constant-buoyancy forcings. As long as a shallowness criterion described in §2.2 is satisfied, our theory applies, in principle, to both anabatic and katabatic flows. However, since katabatic flows are much shallower than anabatic flows, our focus will be on katabatic flows.

The classical Prandtl model describes the flow of a viscous fluid along a uniformly cooled/heated sloping planar surface in a stably stratified fluid. Flow in the model has a boundary-layer character (low-level jet topped by weak reversed flow), and is exact within the Boussinesq framework: along-slope advection of environmental (mean) temperature balances thermal diffusion, along-slope component of buoyancy balances diffusion of along-slope velocity component, and all other terms in the equations of motion and thermodynamic energy are identically zero. Observations suggest that this simple one-dimensional natural convection model can provide a good description of the vertical structure of slope flows at night and a reasonable approximation of slope flows during the day, when the mixing parameters of the model are appropriately tuned (e.g. Defant 1949; Tyson 1968; Papadopoulos *et al.* 1997; Oerlemans 1998). With a suitable change of variables, the Prandtl model also describes the along-slope flow and perturbation salinity field in an oceanic mixing layer at a sloping sidewall (Phillips 1970; Wunsch 1970; Peacock, Stocker & Aristoff 2004). In this oceanic context, the flow is generated solenoidally by isopycnals that are forced to approach the sloping boundary at a right angle (zero normal flux condition). This model also describes the free convective flow of a stratified fluid along heated vertical plates (Gill 1966; Elder 1965; Shapiro & Fedorovich 2004), and the familiar Ekman flow of a homogeneous viscous rotating fluid in the presence of an imposed wind stress or pressure gradient force (Batchelor 1967). The equivalence of the classical Prandtl and Ekman models is a consequence of the general analogy between stratified and rotating flows (Veronis 1970).

The Prandtl model has undergone several extensions within its one-dimensional framework. Gutman & Malbackov (1964), Lykosov & Gutman (1972), Gutman & Melgarejo (1981) and Gutman (1983) made provision for the Coriolis force, external winds, time dependence and simple but non-constant eddy viscosities. Egger (1985) extended the work of Lykosov & Gutman (1972) to include radiative damping. Grisogono & Oerlemans (2001, 2002) considered more general vertical variations in the eddy viscosity and presented solutions valid in the WKB approximation. In the context of oceanic Ekman flows, Madsen (1977) imposed a linearly varying eddy viscosity and made provision for unsteadiness (response to an impulsive surface wind stress). The imposition of non-constant eddy viscosities resulted in more accurate velocity profiles.

For the study of two- and three-dimensional slope flows, a variety of other approaches have been developed. Egger (1981) and Kondo (1984) obtained two-dimensional analytical solutions of governing equations that had been linearized about a state of rest. Despite the limitations of linearity and K-theory with constant coefficients, these solutions yielded qualitatively realistic circulation patterns in the presence of non-uniform surface heating and finite basin size. In the hydraulic approach (Ball 1956; Manins & Sawford 1979; Fitzjarrald 1984; Haiden & Whiteman 2005), the equations of motion, mass conservation and (usually) thermodynamic energy were integrated vertically to obtain layer–mean budget equations. Closure of the hydraulic

model usually involved neglect of some terms, introduction of empirical shape factors, and specification of an entrainment rate at the top of the katabatic layer. The hydraulic model was successfully applied to katabatic jumps (e.g. Ball 1956), and has provided good estimates of the depth of katabatic layers (e.g. Doran & Horst 1983). Advances in computer technology have also made possible three-dimensional numerical mesoscale modelling (Parish 1984; Parish & Waight 1987; Gallee & Schayes 1994; Atkinson 1995; Bromwich *et al.* 2001; Klein *et al.* 2001; Heinemann & Klein 2002; Renfrew 2004) and even large-eddy simulation (Skyllingstad 2003) of katabatic flows.

In this study, we extend the Prandtl model to include surface-buoyancy inhomogeneity. The along-slope surface-buoyancy gradient is treated as a constant parameter. The other parameters of the extended model are slope angle, Brunt–Väisälä frequency, kinematic viscosity and diffusivity, and the homogeneous part of the surface buoyancy. We defer treatment of the Coriolis force, cross-slope motions, an external pressure gradient force and an ambient wind to later studies. The presence of an inhomogeneous surface buoyancy gives rise to acceleration, vertical motions associated with low-level convergence, and horizontal and vertical advection of perturbation buoyancy. Such processes are not accounted for in the classical model.

Although our extended model is two-dimensional and nonlinear, the adoption of a similarity hypothesis (linear dependence of buoyancy and along-slope velocity component on the along-slope coordinate), introduced in §2, allows removal of the along-slope dependence from the governing equations, and greatly simplifies the problem. In particular, the Boussinesq equations of motion and thermodynamic energy in the steady state reduce exactly to a set of coupled nonlinear ordinary differential equations.

The paper is arranged as follows. The governing equations and similarity model are introduced in §2. Solutions for linear and nonlinear free oscillations are presented in §3. In §4, asymptotic solutions of the steady-state equations valid for large values of the slope-normal coordinate are derived for a Prandtl number of unity. The free parameters in these solutions are adjusted to conform to lower boundary conditions of no slip, impermeability and specified surface buoyancy. Formulae are obtained for the boundary-layer thickness and the slope-normal velocity component at the top of the boundary layer (entrainment/detrainment velocity). A criterion for non-existence of steady-state solutions is also obtained. In §5, solutions from nonlinear numerical integrations of an initial-value problem with suddenly imposed surface buoyancy in a fluid initially at rest are presented. The asymptotic solutions are found to be in excellent agreement with these numerical solutions after the steady state has been reached. Key results are summarized in §6.

2. A similarity model for two-dimensional katabatic flow

2.1. *Governing equations*

We consider two-dimensional katabatic flow in the vertical plane aligned with the topographic gradient (figure 1). The flow is governed by the following Boussinesq equations of thermodynamic energy, momentum, and mass conservation:

$$\frac{\partial B}{\partial T} + (\boldsymbol{V} \cdot \nabla)B = -N^2 \boldsymbol{K}^* \cdot \boldsymbol{V} + \kappa \nabla^2 B, \qquad (2.1)$$

$$\frac{\partial \boldsymbol{V}}{\partial T} + (\boldsymbol{V} \cdot \nabla)\boldsymbol{V} = -\nabla \Pi + B\boldsymbol{K}^* + \nu \nabla^2 \boldsymbol{V}, \qquad (2.2)$$
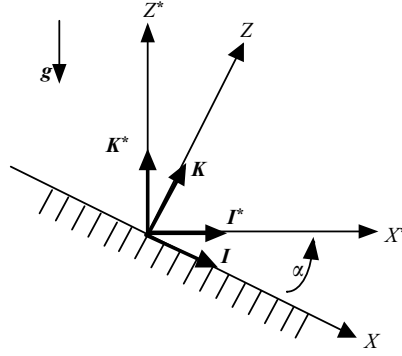
$$\nabla \cdot \boldsymbol{V} = 0. \qquad (2.3)$$

FIGURE 1. Slope-following coordinate system.

Here $\Pi \equiv (P - P_\infty)/\rho_r$ is a normalized perturbation pressure (P is pressure, P_∞ is environmental pressure, which is hydrostatic, ρ_r is a constant reference density), $\boldsymbol{V}$ is the two-dimensional velocity vector, T is time, ν and κ are (constant) eddy viscosity and thermal diffusivity coefficients, respectively, and $\boldsymbol{K}^*$ is the unit vector associated with the Cartesian Z^*-axis, which points in the direction opposite to the gravity vector $\boldsymbol{g}$. The buoyancy is defined as $B \equiv g(\theta - \theta_\infty)/\theta_r$ (θ is potential temperature, θ_∞ is a height-dependent environmental potential temperature, θ_r is a constant reference potential temperature, $g \equiv |\boldsymbol{g}|$), and the Brunt–Väisälä frequency as $N \equiv \sqrt{(g/\theta_r)/\mathrm{d}\theta_\infty/\mathrm{d}Z^*}$. We assume θ_∞ varies linearly with Z^*, so N is constant. The neglect of Coriolis terms is appropriate for flows with Rossby numbers $Ro \equiv V/(fL) \gg 1$ (say, of the order of 10). For speeds characteristic of ordinary katabatic flows ($V \sim 1\,\mathrm{m\,s}^{-1}$ for weak flow, $\sim 10\,\mathrm{m\,s}^{-1}$ for strong flow) at mid- to upper-latitudes (Coriolis parameter $f \sim 10^{-4}\,\mathrm{s}^{-1}$), a Rossby number of 10 is obtained for a horizontal length scale L of $1\,\mathrm{km}$ for weak flow, and $10\,\mathrm{km}$ for strong flow. Thus, our analysis should be appropriate for flows with length scales of those orders. For flows at lower latitudes, larger horizontal length scales may be considered.

The lower boundary is a planar surface inclined at slope angle α with respect to the horizontal. We introduce a slope-following Cartesian coordinate system (X, Z) obtained from the original Cartesian coordinate system (X^*, Z^*) by a rotation through the slope angle (figure 1). The X-axis is the along- (down-) slope coordinate, and the Z-axis is the slope-normal coordinate. The flow variables do not vary in the cross-slope (into page) direction. The unit vectors in the X^*, Z^* directions are $\boldsymbol{I}^*$, $\boldsymbol{K}^*$, respectively, while the corresponding unit vectors in the X, Z directions are $\boldsymbol{I}$, $\boldsymbol{K}$. Writing $\boldsymbol{V}$ as $\boldsymbol{V} = U\boldsymbol{I} + W\boldsymbol{K}$, and noting that $\boldsymbol{K}^*$ projects only in the (X, Z)-plane (so $\boldsymbol{K}^* \cdot \boldsymbol{V} = U\boldsymbol{K}^* \cdot \boldsymbol{I} + W\boldsymbol{K}^* \cdot \boldsymbol{K} = -U\sin\alpha + W\cos\alpha$), (2.1)–(2.3) become

$$\frac{\partial B}{\partial T} + U\frac{\partial B}{\partial X} + W\frac{\partial B}{\partial Z} = UN^2\sin\alpha - WN^2\cos\alpha + \kappa\left(\frac{\partial^2 B}{\partial X^2} + \frac{\partial^2 B}{\partial Z^2}\right), \quad (2.4)$$

$$\frac{\partial U}{\partial T} + U\frac{\partial U}{\partial X} + W\frac{\partial U}{\partial Z} = -\frac{\partial \Pi}{\partial X} - B\sin\alpha + \nu\left(\frac{\partial^2 U}{\partial X^2} + \frac{\partial^2 U}{\partial Z^2}\right), \quad (2.5)$$

$$\frac{\partial W}{\partial T} + U\frac{\partial W}{\partial X} + W\frac{\partial W}{\partial Z} = -\frac{\partial \Pi}{\partial Z} + B\cos\alpha + \nu\left(\frac{\partial^2 W}{\partial X^2} + \frac{\partial^2 W}{\partial Z^2}\right), \quad (2.6)$$

$$\frac{\partial U}{\partial X} + \frac{\partial W}{\partial Z} = 0. \quad (2.7)$$

In terms of the non-dimensional variables

$$x \equiv X \frac{\sin^{3/2}\alpha}{\cos\alpha}\sqrt{\frac{N}{\nu}}, \quad z \equiv Z\sqrt{\frac{N\sin\alpha}{\nu}}, \quad t \equiv TN\sin\alpha, \quad w \equiv \frac{W}{\sqrt{N\sin\alpha\nu}},$$

$$u \equiv \frac{U}{\cos\alpha}\sqrt{\frac{\sin\alpha}{N\nu}}, \quad b \equiv \frac{B}{N\cos\alpha}\sqrt{\frac{\sin\alpha}{N\nu}}, \quad \pi \equiv \frac{\Pi}{N\nu}\frac{\sin\alpha}{\cos^2\alpha}, \quad (2.8)$$

(2.4)–(2.7) become

$$\frac{\partial b}{\partial t} + u\frac{\partial b}{\partial x} + w\frac{\partial b}{\partial z} = u - w + \frac{1}{Pr}\left(\tan^2\alpha\frac{\partial^2 b}{\partial x^2} + \frac{\partial^2 b}{\partial z^2}\right), \quad (2.9)$$

$$\frac{\partial u}{\partial t} + u\frac{\partial u}{\partial x} + w\frac{\partial u}{\partial z} = -\frac{\partial\pi}{\partial x} - b + \tan^2\alpha\frac{\partial^2 u}{\partial x^2} + \frac{\partial^2 u}{\partial z^2}, \quad (2.10)$$

$$\frac{\partial w}{\partial t} + u\frac{\partial w}{\partial x} + w\frac{\partial w}{\partial z} = -\cot^2\alpha\frac{\partial\pi}{\partial z} + \cot^2\alpha b + \tan^2\alpha\frac{\partial^2 w}{\partial x^2} + \frac{\partial^2 w}{\partial z^2}, \quad (2.11)$$

$$\frac{\partial u}{\partial x} + \frac{\partial w}{\partial z} = 0, \quad (2.12)$$

where $Pr \equiv \nu/\kappa$ is the Prandtl number. Since $\sin\alpha$ and $\cos\alpha$ are non-dimensional, any arrangement of them in (2.8) would yield a non-dimensional equation set. Our particular arrangement was chosen, with hindsight, to remove α as a free parameter from the balance equations for the wind and buoyancy variables in the similarity model (see below).

2.2. *The similarity model*

We consider idealized buoyancy fields that vary linearly with the along-slope (x) coordinate. Such distributions may be good local approximations to real buoyancy fields that vary gradually with x. In view of (2.9) and (2.12), an along-slope velocity component u consistent with this buoyancy field should vary linearly with x, and the slope-normal velocity component w should be independent of x. Equations (2.10) and (2.11) then indicate that the pressure can have both linear and quadratic dependences on x, but the quadratic part must be independent of z. The quadratic part corresponds to the case of a stagnation-point flow (Schlichting 1979), but probably has little relevance to katabatic flows, and is therefore dropped from further consideration. Thus, the idealized flow satisfies the following spatial similarity constraint,

$$w = w_0, \quad u = u_0 - x\frac{\partial w_0}{\partial z}, \quad b = b_0 + xb_x, \quad \pi = \pi_0 + x\pi_x, \quad (2.13)$$

where $w_0, u_0, b_0, b_x, \pi_0, \pi_x$ vary with z and t, but are independent of x. Since w itself is independent of x, it will be convenient to simply use 'w' in place of 'w_0'. Note that the expressions for u and w in (2.13) ensure that (2.12) is satisfied.

In the rest of this study, w, b_x and π_x will be referred to as divergent flow variables, while u_0, b_0, and π_0 will be referred to as non-divergent flow variables. As will be shown below, the divergent flow variables are decoupled from the non-divergent flow variables.

Since the $\partial^2/\partial x^2$ diffusion terms in (2.9)–(2.11) vanish identically in the framework of the similarity constraint, the suitability of the constraint in real applications hinges, in part, on when these terms can be safely neglected. A scale analysis shows that these terms are much smaller than the corresponding $\partial^2/\partial z^2$ diffusion terms for small aspect ratios $H/L \ll 1$, where H and L are dimensional length scales in the slope-normal and along-slope directions, respectively. Thus, the constraint should be suitable for

shallow boundary-layer-type flows. Since katabatic winds reach their peak intensity at heights of the order of 1–100 m above ground level, the shallowness criterion should be amply satisfied in many scenarios.

Substituting (2.13) into (2.9)–(2.11), and collecting terms in common powers of x yields

$$\frac{\partial b_0}{\partial t} + u_0 b_x + w \frac{\partial b_0}{\partial z} = u_0 - w + \frac{1}{Pr} \frac{\partial^2 b_0}{\partial z^2}, \tag{2.14}$$

$$\frac{\partial b_x}{\partial t} - b_x \frac{\partial w}{\partial z} + w \frac{\partial b_x}{\partial z} = -\frac{\partial w}{\partial z} + \frac{1}{Pr} \frac{\partial^2 b_x}{\partial z^2}, \tag{2.15}$$

$$\frac{\partial u_0}{\partial t} - u_0 \frac{\partial w}{\partial z} + w \frac{\partial u_0}{\partial z} = -\pi_x - b_0 + \frac{\partial^2 u_0}{\partial z^2}, \tag{2.16}$$

$$\frac{\partial^2 w}{\partial t \partial z} - \left(\frac{\partial w}{\partial z} \right)^2 + w \frac{\partial^2 w}{\partial z^2} = b_x + \frac{\partial^3 w}{\partial z^3}, \tag{2.17}$$

$$\frac{\partial w}{\partial t} + w \frac{\partial w}{\partial z} = \cot^2 \alpha \left(-\frac{\partial \pi_0}{\partial z} + b_0 \right) + \frac{\partial^2 w}{\partial z^2}, \tag{2.18}$$

$$0 = \frac{\partial \pi_x}{\partial z} - b_x. \tag{2.19}$$

The boundary conditions for (2.14)–(2.19) are the remote conditions

$$\lim_{z \to \infty} \left(\frac{\partial w}{\partial z}, b_x, \frac{\partial u_0}{\partial z}, b_0, \pi_0, \pi_x \right) = 0, \tag{2.20}$$

and the surface conditions

$w(0, t) = 0$	(impermeability),	(2.21)
$\dfrac{\partial w}{\partial z}(0, t) = 0$	(no-slip on divergent part of u-velocity),	(2.22)
$b_x(0, t) = b_{xs}$	(specified along-slope buoyancy gradient),	(2.23)
$u_0(0, t) = 0$	(no-slip on non-divergent part of u-velocity),	(2.24)
$b_0(0, t) = b_{0s}$	(specified homogeneous part of surface buoyancy)	(2.25)

The reasons for imposing remote conditions on $\partial w / \partial z$ and $\partial u_0 / \partial z$ instead of w and u_0 will be discussed in §4.

We draw attention to several features of this model.

(i) In proceeding from (2.9)–(2.12) to (2.14)–(2.19), the number of independent variables has been reduced from three, (x, z, t), to two, (z, t). In the steady state, (2.14)–(2.19) further reduce to ordinary differential equations.

(ii) The system (2.14)–(2.19) is exact within the Boussinesq framework, that is, for flows constrained to satisfy the similarity constraint (2.13), the governing equations (2.9)–(2.12) exactly reduce to (2.14)–(2.19). Analogous similarity constraints have led to exact solutions of the Navier–Stokes equations for planar and axisymmetric stagnation-point flows and von Kármán–Bödewadt vortices (Schlichting 1979), to exact solutions of the nonlinear shallow-water equations for basins of elliptical cross-section and parabolic depth variation (Thacker 1981; Cushman-Roisin 1984, 1987; Cushman-Roisin, Heil & Nef 1985; Shapiro 1996), and to nonlinear descriptions of the sea-breeze phenomenon (§ 7.2 of Gutman 1972) and of thermal convection in the layer between two conducting horizontal boundaries (Fiedler 1999).

(iii) A partial decoupling of variables in (2.14)–(2.19) greatly facilitates the solution of these equations. Equations (2.15), (2.17) comprise a closed nonlinear system for two of the divergent flow variables, w and b_x, that can be solved first. Once w and b_x have been obtained, π_x can be recovered from (2.19) and (2.20) as

$$\pi_x = -\int_z^\infty b_x(z', t)\, \mathrm{d}z'. \tag{2.26}$$

Equations (2.14), (2.16) then form a closed linear system for two of the non-divergent flow variables, u_0 and b_0. Once u_0 and b_0 have been obtained, (2.18) can be integrated for π_0.

(iv) The placement of α in (2.8) is such that α does not appear as a free parameter in (2.14)–(2.17) or (2.19). Thus, there are only two degrees of freedom associated with the solution of w and b_x: Pr and the surface boundary value for b_x (along-slope surface-buoyancy gradient b_{xs}). This latter parameter is completely determined by the ratio of along-slope gradient of potential temperature to along-slope gradient of environmental potential temperature

$$b_{xs} = \frac{1}{N^2 \sin \alpha} \frac{\mathrm{d}B}{\mathrm{d}X}\bigg|_{Z=0} = 1 - \frac{\mathrm{d}\theta/\mathrm{d}X}{\mathrm{d}\theta_\infty/\mathrm{d}X}\bigg|_{Z=0}. \tag{2.27}$$

There are also only two degrees of freedom associated with the solution of u_0 and b_0: Pr and the surface boundary value for b_0,

$$b_{0s} = \frac{B_0}{N \cos \alpha} \sqrt{\frac{\sin \alpha}{N\nu}}, \tag{2.28}$$

where B_0 is the homogeneous part of the surface buoyancy. Although α appears in (2.18), it only enters the solution for π_0 as a multiplicative factor.

(v) If $b_{xs} = 0$, the divergent flow variables vanish throughout the flow domain, and (2.14) and (2.16) reduce to the familiar Prandtl model.

3. Free oscillations

Observations of katabatic winds have revealed the existence of low-frequency oscillations, also called surges, superimposed on the mean katabatic flow (Tyson 1968; Doran & Horst 1981; Stone & Hoard 1989; Helmis & Papadopoulos 1996; Monti *et al.* 2002). The periods of these oscillations typically range from a few tens of minutes to a few hours. A search for free oscillations in our system found two simple nonlinear solutions of the divergent flow system: a standing-wave (sloshing or seiching) mode and a propagating mode.

For the special case of a standing wave, in which b_x and $\partial w / \partial z$ are independent of z, (2.15), (2.17) reduce to

$$\frac{\mathrm{d}b_x}{\mathrm{d}t} = -w' + w'b_x, \tag{3.1}$$

$$\frac{\mathrm{d}w'}{\mathrm{d}t} - w'^2 = b_x, \tag{3.2}$$

where $w' \equiv \partial w / \partial z$. The reduction is exact in the sense that the terms lost in progressing from (2.15), (2.17) to (3.1), (3.2) have not been neglected, but vanished identically under the hypothesis that b_x and $\partial w / \partial z$ are independent of z.

In terms of a new variable Ω defined by

$$w' = -\frac{1}{\Omega}\frac{d\Omega}{dt}, \tag{3.3}$$

(3.2) becomes

$$b_x = -\frac{1}{\Omega}\frac{d^2\Omega}{dt^2}, \tag{3.4}$$

and (3.1) reduces, after fortuitous cancellation of nonlinear terms, to

$$\frac{d^3\Omega}{dt^3} + \frac{d\Omega}{dt} = 0, \tag{3.5}$$

which is readily solved. We obtain

$$\frac{\partial w}{\partial z} = -\frac{\cos(t + \delta)}{\beta + \sin(t + \delta)}, \tag{3.6}$$

$$b_x = \frac{\sin(t + \delta)}{\beta + \sin(t + \delta)}, \tag{3.7}$$

where β and δ are constants. The non-dimensional frequency of unity corresponds to a dimensional frequency of $N \sin\alpha$. Because of the presence of the $\sin\alpha$ factor, these oscillations are of relatively low frequency. For a typical atmospheric value of $N = 10^{-2}\,\text{s}^{-1}$, and slope angles of $1°$, $10°$ and $20°$, the periods are approximately $10\,\text{h}$, $1\,\text{h}$ and $0.5\,\text{h}$, respectively, which is in qualitative agreement with the range of published values of oscillation periods in katabatic flows. The amplitude of the oscillations is strongly dependent on β, and becomes singular if $|\beta| \leqslant 1$.

The streamfunction ψ for this oscillation is obtained from (3.6) and $\partial\psi/\partial x = -w$ as

$$\psi = \frac{\cos(t + \delta)}{\beta + \sin(t + \delta)}xz + J(z, t). \tag{3.8}$$

The first term in (3.8) describes a periodic sloshing flow along hyperbolic streamlines $xz = \text{const}$. The J term accounts for the non-divergent response to the divergent oscillation. Unfortunately, we were unable to determine the form of this term.

To help understand the nature of this standing wave, we first consider the linearized version of (3.1) and (3.2) for the phase in which the along-slope surface buoyancy gradient b_{xs} is positive (buoyancy increase down the slope). In (3.2), positive b_{xs} increases slope-normal velocity divergence, $w' > 0$, which is associated with positive slope-normal flow acceleration. In (3.1), a positive slope-normal velocity divergence reduces the value of the along-slope surface-buoyancy gradient. This linear effect, which acts as a restoring mechanism, arises as along-slope flow convergence, associated with positive slope-normal velocity divergence, brings environmental potential temperature isolines closer together. The nonlinear terms in (3.1) and (3.2) modify what would otherwise be simple harmonic motion. In (3.1), ascent acts nonlinearly to increase the magnitude of the along-slope buoyancy gradient regardless of the sign of this gradient. This effect can be visualized if we consider, for example, ascent in the presence of slope-normal isolines of buoyancy (buoyancy may increase or decrease down the slope). Along-slope convergence associated with this ascent draws the buoyancy isolines closer together, increasing the magnitude of the along-slope buoyancy gradient. In (3.2), the nonlinear vertical advection term, which appears as a squared slope-normal velocity divergence, acts to increase the slope-normal velocity divergence regardless of its sign. Since the slope-normal velocity in the standing wave

varies linearly with height, the flow at higher levels is more efficient in momentum transport than the flow at lower levels. Accordingly, the descent associated with slope-normal divergence leads to greater divergence, and ascent associated with slope-normal convergence leads to greater convergence.

Next, consider propagating divergent disturbances of the form $w = w(\zeta)$, $b_x = b_x(\zeta)$, where $\zeta \equiv z - ct$. Applying these forms in the inviscid versions of (2.15), (2.17), yields

$$(c - w)\frac{\mathrm{d}b_x}{\mathrm{d}\zeta} = \frac{\mathrm{d}w}{\mathrm{d}\zeta}(1 - b_x), \tag{3.9}$$

$$\left(\frac{\mathrm{d}w}{\mathrm{d}\zeta}\right)^2 + (c - w)\frac{\mathrm{d}^2 w}{\mathrm{d}\zeta^2} = -b_x. \tag{3.10}$$

The reduction of (2.15), (2.17) to (3.9), (3.10) is not exact since the viscous/diffusivity terms do not vanish identically, but are merely neglected.

Equations (3.9) and (3.10) are nearly the same as the equations for the angular and axial velocities in an axially propagating centrifugal wave in a solid-body-type vortex (Shapiro 2001), and the flow disturbance represented by (3.9), (3.10) can be considered a stratified (gravitational) analogue of that wave. The solution is obtained as

$$w = -c\sqrt{1 - M^2}\sin[k(z - ct)], \tag{3.11}$$

$$b_x = -\frac{\sqrt{1 - M^2}}{M^2}\{\sqrt{1 - M^2} + \sin[k(z - ct)]\} \quad (M^2 < 1). \tag{3.12}$$

Thus, b_x is the sum of its mean value $1 - 1/M^2$ (which is negative), and a wave that propagates with a non-dimensional wavenumber k and phase speed $c = 1/(kM)$. The non-dimensional frequency $\omega = ck = 1/M$ depends on the mean value of b_x, and approaches unity (dimensional frequency of $N\sin\alpha$) in the small-amplitude limit ($M \to 1$).

Although we were unable to obtain the non-divergent flow response to the divergent-mode oscillations described above, the unforced temporal and progressive wave solutions of (2.14), (2.16) are $u_0 = C\cos t$, $b_0 = C\sin t$ and $u_0 = C\sin(kz - t)$, $b_0 = C\cos(kz - t)$, where C is a constant. The dimensional frequency is $N\sin\alpha$ for both types of waves.

Equations (2.14)–(2.17) also admit solutions of the form:

$$b_x = 0, \quad w = -\tilde{a}(t), \quad b_0 = 0, \quad u_0 = -\tilde{a}(t), \tag{3.13}$$

where $\tilde{a}(t)$ is an arbitrary function of time. When written in dimensional form, the combination of terms $u_0 - w$ is seen to represent the actual vertical (K^*) component of the velocity field, and since this combination is zero in (3.13), these solutions represent purely horizontal motions parallel to environmental isotherms. We speculate that waves or other disturbances originating in the boundary layer may have a remote (environmental) signature in the form of these *en masse* horizontal disturbances. This behaviour was found in the temporal decay of the gravity oscillations above the boundary layer in the numerical integrations (§ 5).

4. Asymptotic analysis of katabatic flow in the steady state

4.1. Overview

An asymptotic analysis (valid for large z) of the divergent and non-divergent flow variables is conducted for the steady state. Attention is restricted to a Prandtl number of unity.

The along-slope surface-buoyancy gradient induces an along-slope velocity divergence (or convergence) and associated subsidence (or ascent) through the depth of the boundary layer. The divergence vanishes at infinity, but its integral, the slope-normal velocity component, need not vanish:

$$\int_0^\infty \frac{\partial u}{\partial x}\,\mathrm{d}z = -\int_0^\infty \frac{\partial w}{\partial z}\,\mathrm{d}z = -w(\infty).$$

We will denote this integrated velocity divergence, or, equivalently, the (minus) remote slope-normal velocity component, as $a \equiv -\lim_{z\to\infty} w(z)$. This flow component is analogous to the axial flow that occurs in von Kármán–Bödewadt vortices above the boundary layer in response to centrifugal pumping near the boundary (Schlichting 1979). As we will see, our flows have a boundary-layer character, and the slope-normal velocity component is nearly uniform above the boundary layer. Accordingly, we will often refer to (minus) a as the slope-normal velocity at the top of the boundary layer.

In the limit $z \to \infty$, (2.20) and (2.14) yield $u_0 - w \to 0$, or, since $w \to -a$, $u_0 \to -a$. These u_0 and w terms originate in the thermodynamic energy equation, where they describe along-slope and slope-normal advection of environmental potential temperature, respectively. As $z \to \infty$, these terms cancel. Thus, the remote flow is parallel to the (horizontal) isentropes and causes no potential temperature advection. The existence of fluid layers moving horizontally towards or away from sloping/vertical lateral boundaries has been observed in a variety of stratified fluid flows. For example, the detrainment of boundary-layer air into the environment as a horizontal intrusion at the level of neutral buoyancy has been observed in upslope flow in the laboratory (Fernando *et al.* 2001) and in numerical simulations of air pollutant transport (Lu & Turco 1994). Horizontal intrusions have also been observed in lakes and reservoirs supplied by inflowing river water that was denser than the basin water at the surface, but not so dense that it would descend all the way to the bottom of the basin. Such inflowing water descends the basin sidewall, entrains ambient water, and flows out into the basin as a neutrally buoyant horizontal intrusion (Imberger & Patterson 1990, p. 405). The tendency for stratified fluid to flow nearly horizontally toward an outlet on the sidewall of a reservoir is the basis of the selective withdrawal technique for improving water quality (Imberger & Patterson 1990, p. 392).

The gross behaviour of the flow as described above is illustrated schematically in figure 2. A detailed analysis of the divergent and non-divergent flow variables is presented below.

4.2. Analysis of the divergent flow

With the slope-normal velocity at the top of the boundary layer denoted by $a \equiv -\lim_{z\to\infty} w(z)$, the velocity perturbation component $\phi(z)$ is given by

$$\phi \equiv -w - a. \tag{4.1}$$

The along-slope buoyancy gradient b_x is assumed to vanish at infinity, along with ϕ. For z large enough, ϕ and b_x are sufficiently small that their products can be
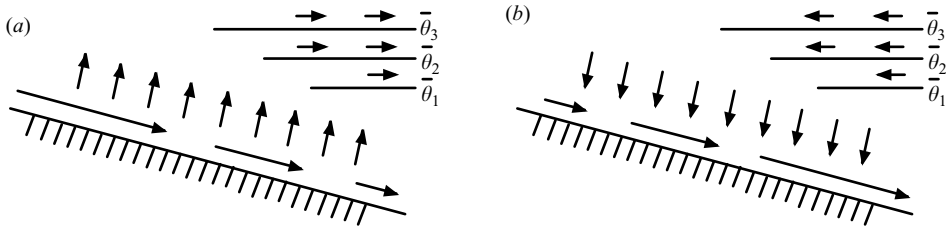
FIGURE 2. Schematic diagrams of katabatic flows in which (*a*) surface buoyancy increases down the slope ($b_{xs} > 0$), and (*b*) surface buoyancy decreases down the slope ($b_{xs} < 0$). An increase in surface buoyancy down the slope yields flow deceleration, convergence, and horizontal along-isentrope intrusion of air into the environment. The sense of the flow is reversed for a surface buoyancy that increases down the slope.

neglected, and (2.15), (2.17) become

$$-ab'_x = \phi' + b''_x, \tag{4.2}$$

$$-a\phi'' = -b_x + \phi'''. \tag{4.3}$$

where a prime denotes differentiation with respect to z. As in treatments of Ekman layers (Batchelor 1967) and one-dimensional slope flows (Gutman & Melgarejo 1981), (4.2), (4.3) can be combined into a single complex equation. Multiplying (4.2) by i and adding the result to (4.3), yields

$$R'' + aR' + iR = 0, \tag{4.4}$$

where

$$R \equiv \phi' + ib_x. \tag{4.5}$$

Solutions of (4.4) are of the form

$$R = A \exp(i\,\varepsilon)\exp(m\,z), \qquad m^2 + a\,m + i = 0, \tag{4.6}$$

where A and ε are real constants. Solving the quadratic equation for m, yields

$$m = -\frac{a}{2} \pm \frac{a}{2}\left(1 + \frac{16}{a^4}\right)^{1/4}\left[\cos\left(\frac{\theta}{2}\right) + i\sin\left(\frac{\theta}{2}\right)\right], \tag{4.7}$$

where θ is such that $\cos\theta = a^2/\sqrt{a^4 + 16}$ and $\sin\theta = -4\sqrt{a^4 + 16}$. Applying the half-angle formulae appropriate for the fourth quadrant ($3\pi/2 < \theta < 2\pi$), $\cos(\theta/2) = -\sqrt{(1 + \cos\theta)/2}$, $\sin(\theta/2) = \sqrt{(1 - \cos\theta)/2}$, introducing the parameter

$$\gamma \equiv \tfrac{1}{2}\sqrt{1 + \frac{16}{a^4}} + \tfrac{1}{2} > 1, \tag{4.8}$$

and choosing the sign in (4.7) to ensure that R vanishes at infinity, transforms (4.7) into

$$m = -\frac{a}{2} - \frac{|a|}{2}\sqrt{\gamma} + i\frac{|a|}{2}\sqrt{\gamma - 1}. \tag{4.9}$$

We then obtain $b_x = \text{Im}(R)$ as

$$b_x = A \exp\left[-\tfrac{1}{2}(a + |a|\sqrt{\gamma})z\right]\sin\left(\frac{|a|}{2}\sqrt{\gamma - 1}\,z + \varepsilon\right). \tag{4.10}$$

Integration of $\phi' = \mathrm{Re}(R)$ yields a similarly compact expression for the perturbation component:

$$\phi = -A\sqrt{\frac{a}{2}(a\gamma - |a|\sqrt{\gamma})}\exp\left[-\tfrac{1}{2}(a + |a|\sqrt{\gamma})z\right]\sin\left(\frac{|a|}{2}\sqrt{\gamma - 1}z + \varepsilon + \delta\right), \quad (4.11)$$

where δ, the phase shift of ϕ relative to b_x, is defined by

$$\cos\delta = \frac{\tfrac{1}{2}(a - |a|\sqrt{\gamma})}{\sqrt{\dfrac{a}{2}(a\gamma - |a|\sqrt{\gamma})}}, \qquad \sin\delta = \frac{\dfrac{|a|}{2}\sqrt{\gamma - 1}}{\sqrt{\dfrac{a}{2}(a\gamma - |a|\sqrt{\gamma})}}. \qquad (4.12)$$

Using $\sqrt{\gamma}\sqrt{\gamma - 1} = 2/a^2$ from (4.8), we obtain

$$\delta \equiv \tan^{-1}\left[-\frac{a}{2}(|a|\sqrt{\gamma} + a\gamma)\right], \qquad \frac{\pi}{2} < \delta < \pi. \qquad (4.13)$$

Care should be taken to ensure that δ appears in the second quadrant ($\pi/2 < \delta < \pi$). For large $|a|$, say, $|a| > 5$, (4.13) is approximated well by $\delta \approx \pi/2$ for $a > 0$ and by $\delta \approx \pi$ for $a < 0$. When evaluating (4.11), it may be more convenient to use (4.12) than (4.13).

These asymptotic solutions are in the form of a spatially decaying oscillation, with the wavelength λ and e-folding decay length scale L_e (which can also be interpreted as a boundary-layer depth scale, see below) given by

$$\lambda = \frac{4\pi}{|a|\sqrt{\gamma - 1}}, \qquad L_e = \frac{2}{a + |a|\sqrt{\gamma}}. \qquad (4.14)$$

For large values of $|a|$, λ is approximated well by $\lambda \approx 2\pi|a|$, while L_e is approximated well by $L_e \approx 1/a$ for $a > 0$, and $L_e \approx |a|^3$ for $a < 0$. For large positive values of a, L_e is very small, indicating rapid decay of b_x and ϕ away from the surface (increasing z). Figure 3(a) depicts λ and L_e for smaller values of $|a|$.

Although the asymptotic analysis is valid for large z, surprisingly accurate formulae for b_x and w_0 (and a) are obtained by extending the solutions down to the surface where the lower boundary conditions apply. Imposing (2.22) and (2.23) on (4.5) yields $R(0) = ib_{xs}$, or, in view of (4.6),

$$\cos\varepsilon = 0, \qquad A\sin\varepsilon = b_{xs}. \qquad (4.15)$$

Applying (2.21) in the form $\phi(0) = -a$, and (4.15) and (4.12) (for $\cos\delta$) in (4.11), yields

$$a = \frac{b_{xs}}{2}(a - |a|\sqrt{\gamma}). \qquad (4.16)$$

Since $\gamma > 1$, (4.16) shows that a and b_{xs} have opposite signs. This is consistent with our expectation that a surface buoyancy increase in the down-slope direction ($b_{xs} > 0$) should yield down-slope weakening of the katabatic winds, and associated flow convergence and rising motion ($w > 0$; $a < 0$).

Using (4.8) for γ, (4.16) is readily solved for the slope-normal velocity at the top of the boundary layer:

$$a = \pm 2\left\{\left[2\left(1 - \frac{2}{b_{xs}}\right)^2 - 1\right]^2 - 1\right\}^{-1/4}, \qquad (4.17)$$

where we take the positive root if $b_{xs} < 0$, and the negative root if $b_{xs} > 0$. Equation (4.17) is shown as a graph in figure 4. This equation yields an intriguing result
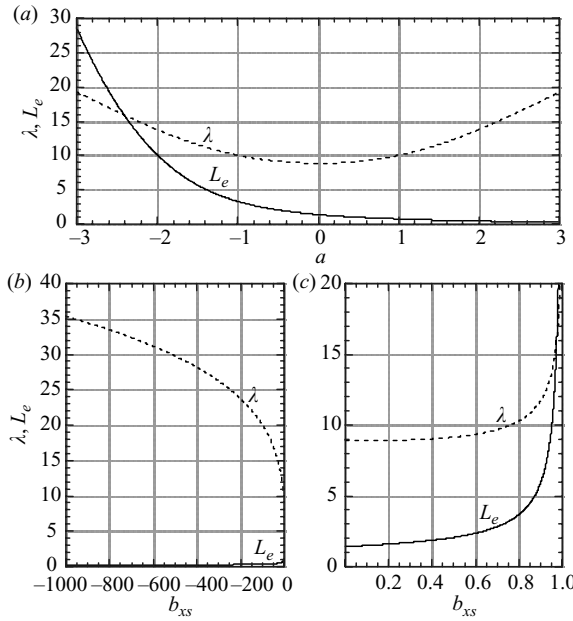
FIGURE 3. Wavelength λ and decay length scale L_e (boundary-layer thickness) from asymptotic theory as functions of: (a) slope-normal velocity at top of boundary layer, a; (b) b_{xs}, for $b_{xs} < 0$; (c) b_{xs}, for $b_{xs} > 0$.
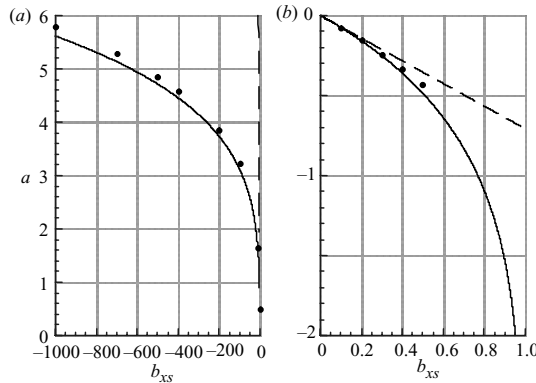

FIGURE 4. Steady-state slope-normal velocity at the top of the boundary layer a as a function of the along-slope surface-buoyancy gradient b_{xs}. The solid curve depicts the asymptotic solution (4.17). Circles show the numerical solution after the transients have died out. The dashed line presents the linear solution $a = -b_{xs}/\sqrt{2}$. Results are shown for $b_{xs} < 0$ in (a), and for $b_{xs} > 0$ in (b).

concerning the existence of solutions. If $b_{xs} > 1$, the quantity in curly brackets is negative, and its $1/4$ root is complex. However, a, which is a velocity component, must be real. This indicates that no steady-state asymptotic solution is possible for $b_{xs} > 1$. In contrast, if we solve the purely linear versions of (2.15), (2.17), that is, (4.2), (4.3) with the terms accounting for slope-normal advection (left-hand sides) set to zero, we obtain $a = -b_{xs}/\sqrt{2}$, which does not breakdown for any value of b_{xs}. Thus, slope-normal advection is necessary for breakdown of the steady state.

The asymptotic solutions with A, ε fixed by (4.15), and a given by (4.17) are

$$b_x = b_{xs} \exp\left(-\frac{z}{L_e}\right) \cos\left(\frac{2\pi z}{\lambda}\right), \tag{4.18}$$

$$w = -a + b_{xs}\sqrt{\frac{a}{2}(-|a|\sqrt{\gamma} + a\gamma)} \exp\left(-\frac{z}{L_e}\right) \cos\left(\frac{2\pi z}{\lambda} + \delta\right), \tag{4.19}$$

$$w' = -b_{xs}\sqrt{\frac{a}{2}(-|a|\sqrt{\gamma} + a\gamma)} \exp\left(-\frac{z}{L_e}\right) \left[\frac{1}{L_e}\cos\left(\frac{2\pi z}{\lambda} + \delta\right)\right.$$
$$\left. + \frac{2\pi}{\lambda}\sin\left(\frac{2\pi z}{\lambda} + \delta\right)\right]. \tag{4.20}$$

The form of these solutions indicates that the decay length scale L_e provides an appropriate measure of the boundary-layer thickness.

When (4.17) is used to replot λ and L_e as functions of b_{xs} (figure 3b, c), the boundary-layer thickness is seen to decrease as b_{xs} decreases in value, and becomes very small for negative values of b_{xs}. In this case, the decay length scale is much smaller than the wavelength, and the oscillations are severely damped. Evidently, the strong subsidence associated with large negative values of b_{xs} results in very shallow non-oscillatory boundary layers.

4.3. Analysis of non-divergent flow

Defining the perturbation along-slope velocity component $\kappa(z)$ by

$$\kappa \equiv u_0 + a, \tag{4.21}$$

and noting that κ, b_0, b_x, and $\phi \to 0$ as $z \to \infty$, (2.14) and (2.16) with π_x supplied from (2.26) can be approximated as

$$-ab_x - ab_0' = \kappa + \phi + b_0'', \tag{4.22}$$

$$-a\phi' - a\kappa' = \int_z^\infty b_x(z')\mathrm{d}z' - b_0 + \kappa''. \tag{4.23}$$

Equations (4.22) and (4.23) combine into the single equation,

$$Q'' + aQ' + iQ = -aR - i\int_\infty^z R(z')\,\mathrm{d}z', \tag{4.24}$$

where

$$Q \equiv \kappa + ib_0, \tag{4.25}$$

and R has been defined in (4.5). Applying (4.6) in (4.24), yields

$$Q'' + aQ' + iQ = mA\exp(mz + i\varepsilon). \tag{4.26}$$

A particular solution Q_p of (4.26) is

$$Q_p = Dz\exp(mz + i\varepsilon), \tag{4.27}$$

where $D = Am/(2m + a)$. In view of (4.9), D can be rationalized and expressed in polar form as

$$D = \frac{A}{2}\frac{|a|}{a}\sqrt{\frac{2\sqrt{\gamma}}{2\gamma - 1}\left(\sqrt{\gamma} + \frac{a}{|a|}\right)}\exp(i\mu), \tag{4.28}$$

where

$$\mu \equiv \tan^{-1}\left[\frac{|a|\sqrt{\gamma-1}}{a(2\gamma-1)+|a|\sqrt{\gamma}}\right] \qquad \begin{array}{l} \text{for } a > 0: 0 < \mu < \dfrac{\pi}{2}, \\[2mm] \text{for } a < 0: \dfrac{\pi}{2} < \mu < \pi. \end{array} \qquad (4.29)$$

Care should be taken in the evaluation of the inverse tangent in (4.29) to ensure that if $a > 0$, μ appears in the first quadrant ($0 < \mu < \pi/2$), but if $a < 0$, μ appears in the second quadrant ($\pi/2 < \mu < \pi$). For large $|a|$, (4.29) is approximated well by $\mu \approx 0$ for $a > 0$, and by $\mu \approx \pi/2$ for $a < 0$.

Affixing the homogeneous solution to the particular solution, we obtain Q as

$$Q = E\exp(mz + i\Lambda) + \frac{A}{2}\frac{|a|}{a}\sqrt{\frac{2\sqrt{\gamma}}{2\gamma-1}}\left(\sqrt{\gamma}+\frac{a}{|a|}\right)z\exp(mz + i\varepsilon + i\mu), \qquad (4.30)$$

where E and Λ are real constants. As in the divergent flow equations (4.18)–(4.20), the non-divergent flow variables oscillate with a wavelength λ given by (4.14). Since the envelope of the waves associated with the particular solution in (4.30) is $Q_{env} \equiv z\exp(-z/L_e)$, with L_e given by (4.14), these waves amplify prior to decaying with z. In contrast, the envelope of the b_x, w waves provides only exponential decay. Setting the first and second derivatives of Q_{env} to zero yields the locations of the envelope maximum and inflection point as L_e and $2L_e$, respectively. An envelope width L_w defined as the distance between these points is equal to L_e. Thus, figure 3(a) also applies to the wavelength and envelope width for the non-divergent flow variables.

If we extend (4.30) down to the surface where (2.24), (2.25) apply, we obtain

$$E = \sqrt{a^2 + b_{0s}^2}, \qquad \cos\Lambda = \frac{a}{E}, \qquad \sin\Lambda = \frac{b_{0s}}{E}, \qquad (4.31)$$

and the solutions for $u_0 = -a + \mathrm{Re}(Q)$ and $b_0 = \mathrm{Im}(Q)$, with E, Λ fixed by (4.31), A, ε fixed by (4.15), and a given by (4.17) are

$$u_0 = -a - \frac{b_{xs}}{2}\frac{|a|}{a}\sqrt{\frac{2\sqrt{\gamma}}{2\gamma-1}}\left(\sqrt{\gamma}+\frac{a}{|a|}\right)\sin\left(\frac{2\pi z}{\lambda}+\mu\right)z\exp\left(-\frac{z}{L_e}\right)$$
$$+ \left[a\cos\left(\frac{2\pi z}{\lambda}\right)-b_{0s}\sin\left(\frac{2\pi z}{\lambda}\right)\right]\exp\left(-\frac{z}{L_e}\right), \quad (4.32)$$

$$b_0 = \frac{b_{xs}}{2}\frac{|a|}{a}\sqrt{\frac{2\sqrt{\gamma}}{2\gamma-1}}\left(\sqrt{\gamma}+\frac{a}{|a|}\right)\cos\left(\frac{2\pi z}{\lambda}+\mu\right)z\exp\left(-\frac{z}{L_e}\right)$$
$$+ \left[a\sin\left(\frac{2\pi z}{\lambda}\right)+b_{0s}\cos\left(\frac{2\pi z}{\lambda}\right)\right]\exp\left(-\frac{z}{L_e}\right). \quad (4.33)$$

5. Numerical integration of the nonlinear system

The structure of the divergent and non-divergent flow variables in the steady state is sought as the terminal state of an initial-value problem in which the flow starts from resting stratification, and the surface buoyancy (along-slope buoyancy gradient and homogeneous part of the buoyancy) is suddenly imposed. We obtain these solutions by numerical integration. Results are presented for a Prandtl number of unity.

5.1. *Numerical solution of the divergent flow system*

The initial-value problem is solved with a version of the forward time centred space (FTCS) finite-difference algorithm (Fletcher 1988). Rather than work directly with w, we introduce $F \equiv -\partial w/\partial z$, in terms of which w becomes $w = -\int_0^z F \, \mathrm{d}z'$. The FTCS approximation of (2.15), (2.17) on a uniform grid with trapezoidal rule for discretization of $\int_0^z F \, \mathrm{d}z'$ yields the algorithm:

$$b_{xm}^{n+1} = b_{xm}^n + \Delta t \left(1 - b_{xm}^n\right) F_m^n + 0.5 \Delta t I_m^n \left(b_{xm+1}^n - b_{xm-1}^n\right)$$
$$+ \frac{s}{Pr}\left(b_{xm+1}^n - 2b_{xm}^n + b_{xm-1}^n\right), \quad (5.1)$$

$$F_m^{n+1} = F_m^n - \Delta t \left(F_m^n\right)^2 + 0.5 \Delta t I_m^n \left(F_{m+1}^n - F_{m-1}^n\right) - \Delta t b_{xm}^n$$
$$+ s\left(F_{m+1}^n - 2F_m^n + F_{m-1}^n\right), \quad (5.2)$$

where

$$I_m^n = -\frac{w_m^n}{\Delta z}. \quad (5.3)$$

and

$$\left.\begin{aligned} I_m^n &= I_{m-1}^n + 0.5\left(F_{m-1}^n + F_m^n\right) \quad (m \geqslant 2), \\ &= 0 \quad\quad\quad\quad\quad\quad\quad\quad\quad (m = 1). \end{aligned}\right\} \quad (5.4)$$

Here, a superscript n is a time index, a subscript m is a space index, Δt is the time step, Δz is the grid spacing, and $s \equiv \Delta t/\Delta z^2$. For the results presented here, $s = 0.5$ and $\Delta z = 0.04$. The boundary values are obtained from (2.20)–(2.23), and the initial conditions are of no motion and no thermal perturbations. In (2.20), we take infinity to be top of the computational domain, $m = m_{max}$, where the total number of grid points, m_{max}, is large enough that any further increase in its value produces negligible change to the flow variables throughout the computational domain. The value $m_{max} = 501$ was found to be acceptable for the experiments described here.

For all numerical experiments with negative values of b_{xs} (prescribed between -0.1 and -1000), a steady state was obtained after gravity-wave transients had died out. In contrast, for the experiments in which positive values of b_{xs} were prescribed, a steady state was not found if b_{xs} exceeded a threshold value b_{xs}^* in the range $0.54 < b_{xs}^* < 0.58$, somewhat less than the value of 1 in the asymptotic theory. As b_{xs} approached the threshold value from below, the gravitational oscillations that developed in the solution grew to larger amplitude, and took longer to damp out. This behaviour is illustrated in figure 5, which depicts oscillations in w at a fixed location $z = 6$ for three representative sub-threshold values of b_{xs} (0.5, -0.5, -5). This location was above the boundary layer for all times in the $b_{xs} = -0.5, -5$ experiments, but it was not clear that a boundary layer even existed in the $b_{xs} = 0.5$ experiment until after the transients had died out. For values of b_{xs} above the threshold value, the oscillations increased in amplitude, and the numerical solution eventually became unstable. A phase portrait of $b_x = b_x[w(t)]$ at a fixed location for two values of b_{xs} bracketing the threshold value suggests the existence of an unstable limit cycle (figure 6). Detailed inspection of the solution curves for w and b_x at early times in the integrations (not shown) indicated that for negative b_{xs}, the oscillatory temporal decay above the boundary layer was largely in the form of an *en masse* disturbance (3.13). In contrast, for $b_{xs} = 0.5$, the solution throughout much of the domain at early times
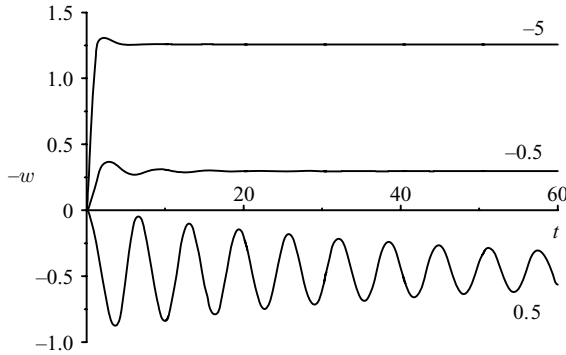
FIGURE 5. Transient behaviour of w at a fixed location $z = 6$ for three values of the along-slope surface-buoyancy gradient: $b_{xs} = -5$ (top curve), $b_{xs} = -0.5$ (middle curve), $b_{xs} = 0.5$ (lower curve). In the latter case, a steady state was reached after a much longer integration period than displayed in the plot.
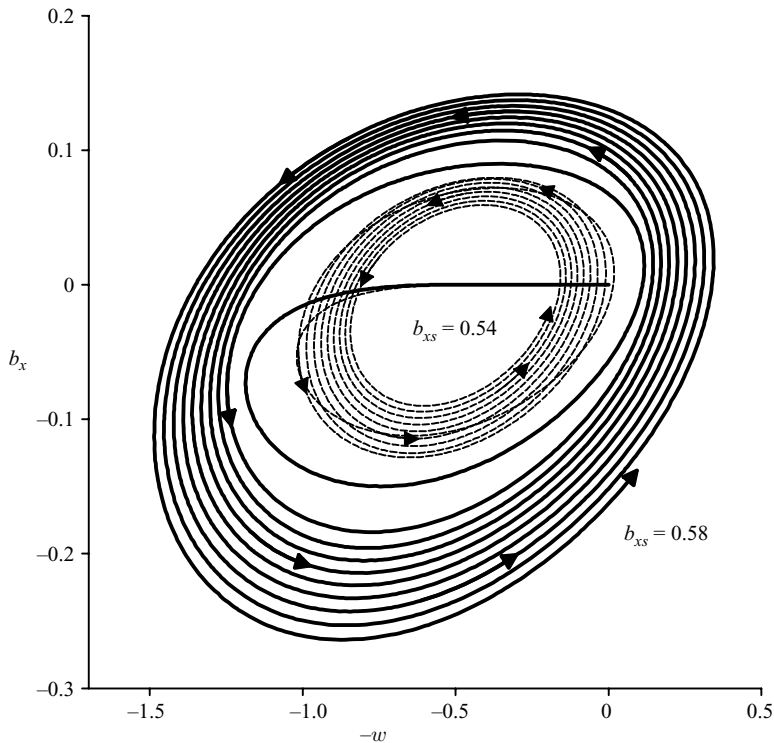

FIGURE 6. Trajectory in $w - b_x$ space at $z = 6$ for $b_{xs} = 0.58$ (solid curve) and $b_{xs} = 0.54$ (dashed curve). These curves suggest the existence of an unstable limit cycle.

was similar to the temporal oscillation (3.6), (3.7) that is, w and b_x had a frequency of unity (period of 2π), w varied linearly with z, and b_x was largely independent of z (and non-zero). In this latter experiment, a boundary-layer-type flow was not obtained until these disturbances had died out.

One of the referees has proposed a Lagrangian (air parcel) viewpoint for understanding the preferential development of waves in the experiments with positive
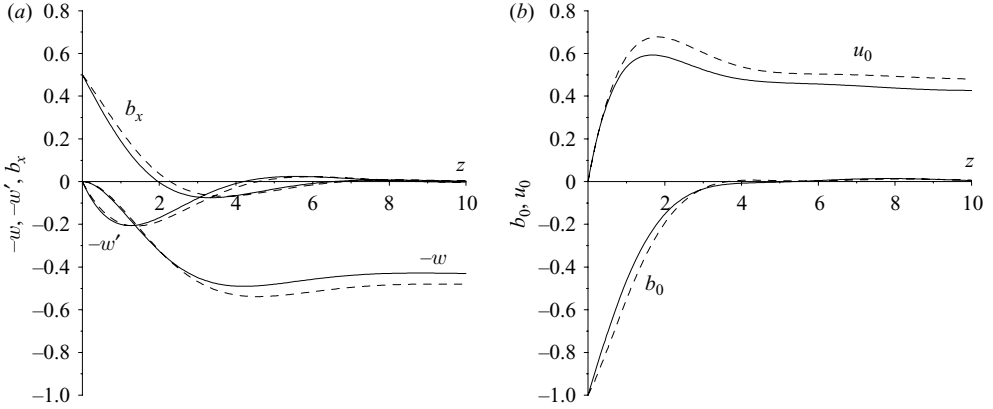
FIGURE 7. Flow variables in the steady state as functions of z for $b_{xs} = 0.5$ and $b_{0s} = -1$. (a) The divergent flow variables $-w$, $-w'$, b_x. (b) The non-divergent flow variables b_0, u_0. Solid curves present the numerical solutions. Dashed curves show the asymptotic solutions.
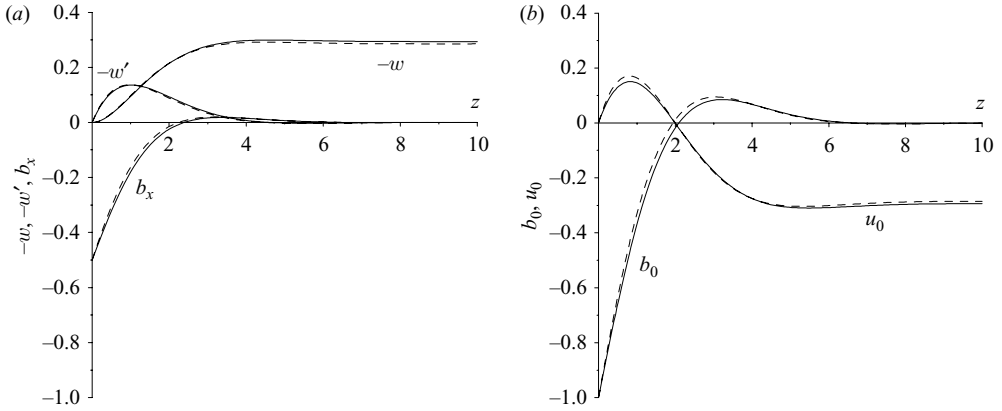

FIGURE 8. As in figure 7, but for $b_{xs} = -0.5$ and $b_{0s} = -1$.

values of b_{xs}. In the case of positive b_{xs}, parcels in the lower part of the boundary layer acquire buoyancy through surface forcing (mediated by diffusion), ascend through the depth of the boundary layer (positive b_{xs} is associated with down-slope weakening of the katabatic forcing, and thus along-slope convergence), and are then ejected into the environment. These parcels overshoot their equilibrium level and participate in buoyancy oscillations. In contrast, in the case of negative b_{xs}, neutrally buoyant environmental parcels are sucked into the boundary layer where they fall under the control of surface forcing. Although these parcels eventually acquire buoyancy, they do so only after they are trapped in the boundary layer, and so are unable to participate in significant buoyancy oscillations.

We now focus on the steady state. For negative values of b_{xs} and for positive values of b_{xs} less than the threshold, excellent agreement is found between the steady-state slope-normal velocity at the top of the boundary layer obtained from the asymptotic theory and from the numerical integrations (figure 4). More generally, very good agreement is found between the steady-state numerical and asymptotic solutions for w and b_x throughout the flow domain. Results for $b_{xs} = 0.5, -0.5, -5$, are presented in figures 7–9. These figures show the boundary-layer character of the divergent
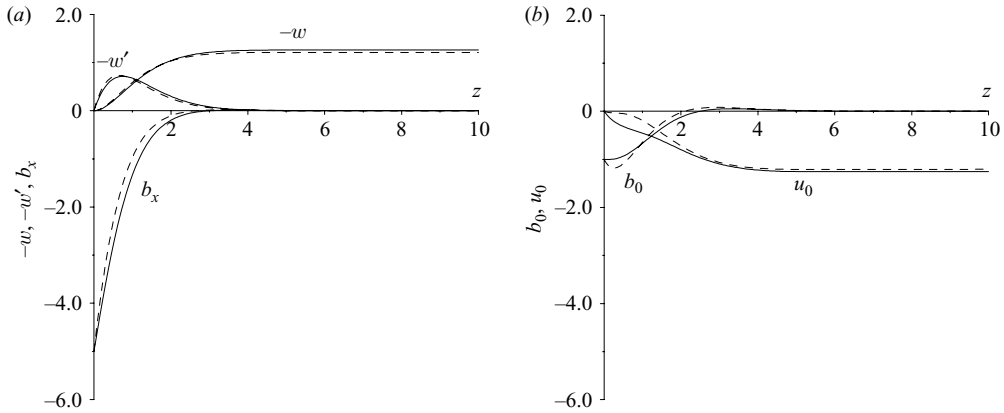
FIGURE 9. As in figure 7, but for $b_{xs} = -5$ and $b_{0s} = -1$.

flow variables (with superimposed decaying spatial oscillations that become apparent for positive values of b_{xs}) and the nearly uniform slope-normal velocity component above the boundary layer. They also show the thickening of the boundary layer with increasing values of b_{xs}, consistent with the asymptotic theory.

The greatest deviation between the asymptotic and numerical solutions appears in the solution for w at large z. It should be recalled that the plotted asymptotic solutions have been adjusted to conform to the lower boundary conditions. The adjustment leads to accurate descriptions of w, w', b_x throughout the flow domain (beyond their original domain of validity), but at the slight expense of the accuracy of the remote solution for w.

Data from the final integration time were used to evaluate the forcing terms in the thermodynamic equation (2.15) and equation of motion (2.17). Figures 10–12 depict these terms for the values of b_{xs} considered in figures 7–9. For these (and other) values of b_{xs}, the largest terms in (2.17) are w''' and b_x, which account for momentum diffusion and buoyancy. The nonlinear acceleration terms in (2.17) are relatively small, and remain small even for b_{xs} ranging down to -1000. In contrast, the relative magnitudes of the terms in (2.15) are strongly dependent on b_{xs}. For small magnitudes of $b_{xs} (0.5, -0.5)$ the dominant balance is between w' and b''_x, that is, between along-slope advection of environmental potential temperature and diffusion of along-slope buoyancy gradient. However, it can be noted that even though the nonlinear terms in (2.15) and (2.17) are relatively small for $b_{xs} = 0.5$ in the steady-state (and are not dominant in the transient solution) they are responsible for the self-excitation of gravity waves in the numerical solution leading to the steady state, and lead to the breakdown of the solution for values of b_{xs} only slightly greater than 0.5 (e.g. 0.58). For the larger-magnitude case, $b_{xs} = -5$, the nonlinear terms wb'_x and $b_x w'$ (accounting for along-slope and slope-normal advection of the buoyancy gradient) become larger than w', with all three opposing the largest term, b''_x. In other experiments, as negative b_{xs} becomes progressively larger in magnitude, w' becomes negligible, and the (large) nonlinear terms act in concert to oppose b''_x. Confirmation of the importance of the slope-normal advection terms at large magnitudes of (negative) b_{xs} comes from figure 4(a), where the purely linear solution (nearly vertical dashed line) differs dramatically from both the numerical solution and the asymptotic solution.
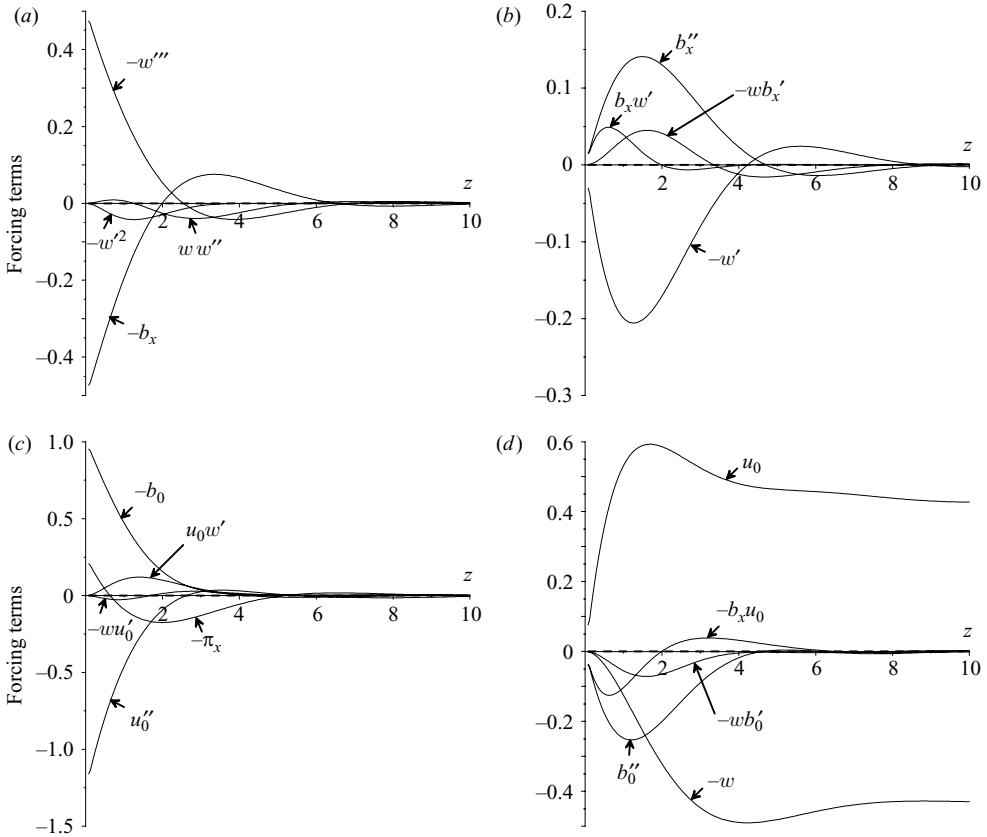
FIGURE 10. Terms in the balance equations for w [(2.17), (a)], b_x [(2.15), (b)], u_0 [(2.16), (c)] and b_0 [(2.14), (d)] for $b_{xs} = 0.5$ and $b_{0s} = -1$. The sum of the terms in each figure, shown by the dashed line almost coincident with the z-axis, is nearly zero, indicating the flow is in a steady state.

Other numerical experiments reveal that the structure of the steady-state solution is independent of the manner in which the surface forcing is imposed, that is, whether b_{xs} is imposed impulsively or is gradually ramped up to its full value after a period of time. Moreover, the existence (and numerical value) of a threshold b_{xs}^* for breakdown of the steady state and the self-excitation of gravity waves for b_{xs} values near this threshold are found to be independent of the manner (impulsive or continuous) in which the surface forcing is imposed. The breakdown threshold and self-excitation phenomenon are also found to be insensitive to increases in the computational domain (doubling m_{max}) and to changes in the nature of the top boundary conditions (replacing $\partial w / \partial z = 0$, $b_x = 0$ with $\partial^2 w / \partial z^2 = 0$, $\partial b_x / \partial z = 0$), although the solution details in these cases do change near the top boundary. As one of the examples of these sensitivity experiments, we present the slope-normal velocity component w as a function of time at a fixed location for a case where b_{xs} is ramped up gradually (linearly with time) to a value just exceeding the threshold b_{xs}^* (figure 13). In this case, gravity waves do not develop until shortly after the threshold value is exceeded. After that time, waves develop spontaneously.
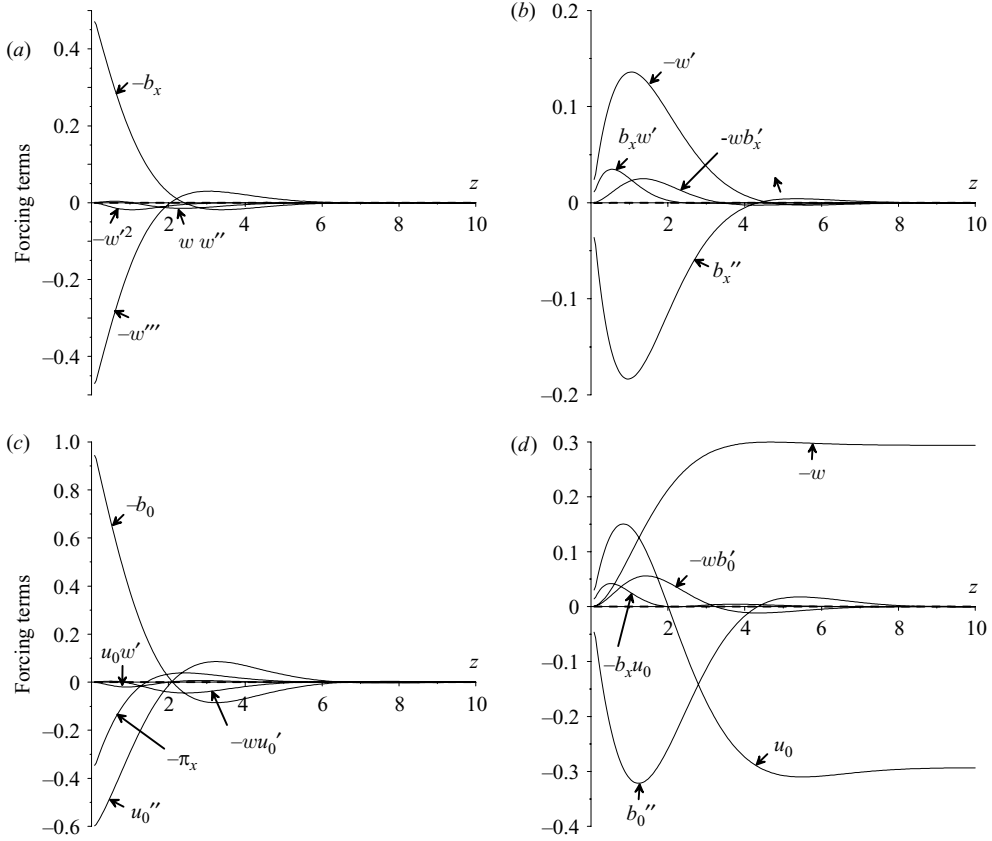
FIGURE 11. As in figure 10, but for $b_{xs} = -0.5$ and $b_{0s} = -1$.

5.2. *Numerical solution of the non-divergent flow system*

The FTCS discretization of (2.14), (2.16) with π_x supplied from (2.26) yields the algorithm,

$$b_{0m}^{n+1} = b_{0m}^n + \Delta t u_{0m}^n \left(1 - b_{xm}^n\right) + 0.5\Delta t I_m^n \left(b_{0m+1}^n - b_{0m-1}^n\right)$$
$$+ \Delta t \Delta z I_m^n + \frac{s}{Pr}\left(b_{0m+1}^n - 2b_{0m}^n + b_{0m-1}^n\right), \quad (5.5)$$

$$u_{0m}^{n+1} = u_{0m}^n \left(1 - \Delta t F_m^n\right) + 0.5\Delta t I_m^n \left(u_{0m+1}^n - u_{0m-1}^n\right) + \Delta t \left(G_\infty^n - G_m^n\right)$$
$$- \Delta t b_{0m}^n + s \left(u_{0m+1}^n - 2u_{0m}^n + u_{0m-1}^n\right), \quad (5.6)$$

where

$$\begin{aligned} G_m^n &= G_{m-1}^n + 0.5\Delta z \left(b_{xm-1}^m + b_{xm}^m\right) & (m \geqslant 2), \\ &= 0 & (m = 1), \end{aligned} \quad (5.7)$$

and other notation is the same as in (5.1)–(5.2). In (5.6), we set G_∞^n equal to the value of G_m^n at the top of the computational domain, $m = m_{max}$. The boundary conditions are (2.20), (2.24) and (2.25), and the initial conditions are of no motion and no thermal perturbation.
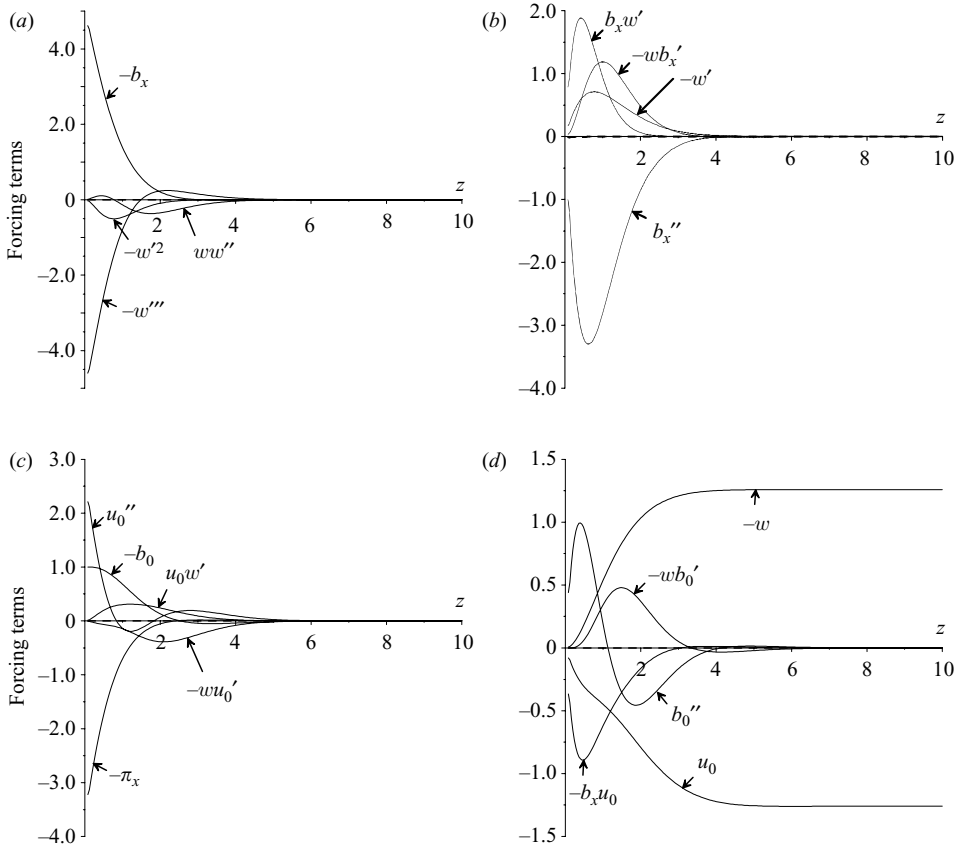
FIGURE 12. As in figure 10, but for $b_{xs} = -5$ and $b_{0s} = -1$.

Experiments showed that the behaviour of the solution and the forcing terms were complicated and depended strongly on the values of b_{xs} and b_{0s}, although in all cases the sum $-w + u_0$ approached zero outside the boundary layer (horizontal flow toward/away from the boundary layer). Results from experiments with $b_{0s} = -1$ and $b_{xs} = 0.5, -0.5, -5$ are presented in figures 7–9. The corresponding forcing terms in (2.14) and (2.16) are presented in (c) and (d) of figures 10–12. Figures 7 and 8 depict a very good agreement between the asymptotic and numerical solutions for $b_{xs} = 0.5$, -0.5, but larger relative errors become evident in figure 9 for $b_{xs} = -5$. These and other experiments show that the relative errors in the asymptotic solutions for b_0, u_0 increase as the magnitude of b_{xs} increases relative to that of b_{0s}. This is not surprising since, according to (2.16), u_0 is linearly forced by both b_0 and b_x (b_x appears in π_x through (2.26)). Thus, for the non-divergent flow variables, we conclude that the asymptotic theory provides a very good approximation to the nonlinear solution as long as b_{0s} is larger than b_{xs}.

6. Summary

The classical Prandtl model for katabatic flow of a stably stratified fluid along a planar surface has been extended to the case where the surface buoyancy varies linearly with distance down the slope − the simplest framework for studying the effect
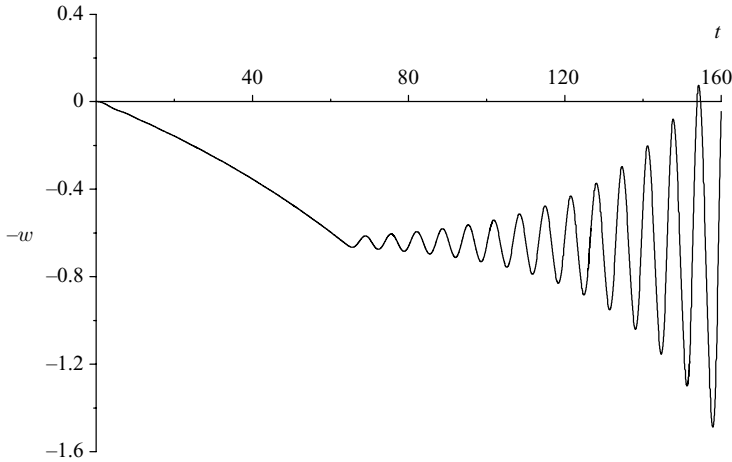
FIGURE 13. Slope-normal velocity w at a fixed location $z = 6$ for the case where the along-slope surface-buoyancy gradient b_{xs} is imposed gradually (linearly) with time, up to a peak value of $b_{xs} = 0.65$ (reached at time $t = 64$).

of surface inhomogeneity. A similarity model in which the buoyancy and along-slope velocity fields vary linearly with distance down the slope was shown to be appropriate in this case. The model removes the explicit along-slope dependence. In the steady state, the similarity constraint reduces the two-dimensional Boussinesq equations of motion, thermodynamic energy and mass conservation to a set of nonlinear ordinary differential equations for divergent-flow variables (along-slope buoyancy and pressure gradient, velocity divergence) and to linear ordinary differential equations for non-divergent flow variables (homogeneous part of the buoyancy, velocity and pressure fields). The governing non-dimensional parameters in this similarity model are the along-slope surface buoyancy gradient, b_{xs} (which accounts for the surface inhomogeneity), the homogeneous part of the surface buoyancy, b_{0s}, (the conventional surface forcing in the classical Prandtl katabatic model), and the Prandtl number.

An asymptotic analysis of the steady state, valid for large distances above the boundary, is conducted for a Prandtl number of unity. The undetermined parameters in the asympotic solutions are adjusted to conform to appropriate surface boundary conditions (no-slip, impermeability and specified buoyancy). The behaviour of the solutions is strongly dependent on the value of the along-slope surface-buoyancy gradient b_{xs}. The unsteady problem is solved numerically, and its terminal-state solutions (after transients have died out) are compared to the asymptotic solutions. The asymptotic solutions for the divergent flow variables are found to be in very good agreement with the corresponding numerical results throughout the domain. The asymptotic solutions for the non-divergent flow variables are found to be in good agreement with the corresponding numerical results, as long as the homogeneous part of the surface buoyancy b_{0s} is larger in magnitude than b_{xs}.

The main features of our inhomogeneous katabatic flow model can be summarized as follows.

(i) A surface-buoyancy decrease in the down-slope direction ($b_{xs} < 0$; down-slope strengthening of katabatic forcing), yields along-slope flow acceleration, and associated subsidence which induces horizontal along-isentrope entrainment of environmental air into the boundary layer. A surface-buoyancy increase in the

down-slope direction ($b_{xs} > 0$; down-slope weakening of katabatic forcing) yields along-slope flow deceleration, and rising motion throughout the boundary layer. Air detrained from the boundary layer intrudes horizontally into the environment.

(ii) The asymptotic theory yields a formula for the slope-normal velocity component at the top of the boundary layer as a function of b_{xs}. The formula is in excellent agreement with values obtained from numerical integration of the similarity equations.

(iii) Steady-state solutions for the divergent flow variables exhibit a boundary-layer character, with the thickness of the boundary layer increasing with b_{xs}. Above the boundary layer, the divergent flow variables undergo an oscillatory spatial decay away from the slope. However, this oscillatory behaviour is apparent only for $b_{xs} > 0$. For $b_{xs} < 0$, as b_{xs} decreases in value (increases in magnitude), the decay length scale for the oscillation becomes much smaller than the wavelength, and the oscillatory behaviour becomes imperceptible. The strong subsidence associated with large negative values of b_{xs} results in a very shallow effectively non-oscillatory boundary layer. The steady-state solutions for the non-divergent flow variables also exhibit a boundary-layer character, but these solutions are generally more complicated than those for the divergent flow variables. Above the boundary layer, both divergent and non-divergent velocity components become uniform and combine to form a horizontal (along-isentrope) flow toward/away from the boundary layer.

(iv) The divergent and non-divergent flow variables approach a steady state through an oscillatory temporal decay with a dimensional frequency of $N \sin\alpha$ (low-frequency gravity waves). However, the temporal oscillations are much more pronounced in the cases where b_{xs} is positive. In such cases, air parcels in the convergent ascent are ejected from the boundary layer into the environment where they overshoot their equilibrium level and participate in buoyancy oscillations. In contrast, in cases of negative b_{xs}, neutrally buoyant environmental parcels are sucked into the boundary layer where their vertical displacements are subsequently curtailed.

(v) Steady-state solutions are obtained for negative values of b_{xs}, but no steady-state solution exists if b_{xs} exceeds a positive threshold b_{xs}^* ($b_{xs}^* = 1$ in the asymptotic solution, $0.54 < b_{xs}^* < 0.58$ in the numerical solution).

(vi) As b_{xs} approaches the threshold value from below, the low-frequency oscillations that develop in the flow grow to larger amplitude, and take longer to damp out. This suggests the possibility that even non-periodic (in space or time) surface-buoyancy inhomogeneity may lead to spontaneous generation (self-excitation) of low-frequency gravity waves in katabatic flows.

(vii) For b_{xs} above the threshold value, the self-excited oscillations increase in amplitude, and the numerical solution eventually becomes unstable.

Future work will focus on numerical simulation of the transition from laminar to turbulent flow regimes and the turbulence structure of inhomogeneous katabatic flows. We will also determine whether processes that might, in principle, be included within the similarity framework (e.g. Coriolis force, cross-slope flow, externally imposed pressure gradient force, ambient winds, or height-dependent eddy viscosities) could delay or preclude the onset of wave development and instability, or whether the similarity constraint would need to be relaxed in order to see how the instability manifests itself in nature. Clearly, the similarity constraint is inconsistent with the existence of hydraulic jumps and related phenomena known to occur with strongly decelerating katabatic flows (Ball 1956; Lied 1964; Pettré & André 1991). It is also possible that the instability marks the onset of a form of convection since $b_{xs} > 0$ eventually leads to a reversal of sign of the buoyancy flux down the slope. Three-dimensional numerical simulation of inhomogeneous flow without a similarity

constraint may be required to study these issues. We will also examine the extent to which the similarity framework can be applied to the so-called stagnation front, a convergent structure that sometimes forms along slopes during the evening transition from anabatic to katabatic conditions (Hunt, Fernando & Princevac 2003; Brazel *et al.* 2005).

REFERENCES

ATKINSON, B. W. 1995 Orographic and stability effects on valley-side drainage flows. *Boundary-Layer Met.* **75**, 403–428.

BALL, F. K. 1956 The theory of strong katabatic winds. *Austral. J. Phys.* **9**, 373–386.

BATCHELOR, G. K. 1967 *An Introduction to Fluid Dynamics.* Cambridge University Press.

BRAZEL, A. J., FERNANDO, H. J. S., HUNT, J. C. R., SELOVER, N., HEDQUIST, B. C. & PARDYJAK, E. 2005 Evening transition observations in Phoenix, Arizona. *J. Appl. Met.* **44**, 99–112.

BROMWICH, D. H., CASSANO, J. J., KLEIN, T., HEINEMANN, G., HINES, K. M., STEFFEN, K. & BOX, J. E. 2001 Mesoscale modeling of katabatic winds over Greenland with the Polar MM5. *Mon. Weather Rev.* **129**, 2290–2309.

CUSHMAN-ROISIN, B. 1984 An exact analytical solution for a time-dependent, elliptical warm-core ring with outcropping interface. *Ocean Modelling* **59**, 5–6.

CUSHMAN-ROISIN, B. 1987 Exact analytical solutions for elliptical vortices of the shallow-water equations. *Tellus* **39** A, 235–244.

CUSHMAN-ROISIN, B., HEIL, W. H. & NOF, D. 1985 Oscillations and rotations of elliptical warm-core rings. *J. Geophys. Res.* **90**, 11 756–11 764.

DEFANT, F. 1949 Zur Theorie der Hangwinde, nebst Bemerkungen zur Theorie der Berg- und Talwinde. *Arch. Met. Geophys. Bioklim.* A **1**, 421–450.

DORAN, J. C. & HORST, T. W. 1981 Velocity and temperature oscillations in drainage winds. *J. Appl. Met.* **20**, 361–364.

DORAN, J. C. & HORST, T. W. 1983 Observations and models of simple nocturnal slope flows. *J. Atmos. Sci.* **40**, 708–717.

ELDER, J. W. 1965 Laminar free convection in a vertical slot. *J. Fluid Mech.* **23**, 77–98.

EGGER, J. 1981 On the linear two-dimensional theory of thermally induced slope winds. *Beitr. Z. Phys. Atmos.* **54**, 465–481.

EGGER, J. 1985 Slope winds and the axisymmetric circulation over Antarctica. *J. Atmos. Sci.* **42**, 1859–1867.

FERNANDO, H. J. S., LEE, S. M., ANDERSON, J., PRINCEVAC, M., PARDYJAK, E. & GROSSMAN-CLARKE, S. 2001 Urban fluid mechanics: air circulation and contaminant dispersion in cities. *Environ. Fluid Mech.* **1**, 107–164.

FIEDLER, B. H. 1999 Thermal convection in a layer bounded by uniform heat flux: application of a strongly nonlinear analytical solution. *Geophys. Astrophys. Fluid Dyn.* **91**, 223–250.

FITZJARRALD, D. R. 1984 Katabatic wind in opposing flow. *J. Atmos. Sci.* **41**, 1143–1158.

FLETCHER, C. A. J. 1988 *Computational Techniques for Fluid Dynamics*, vol. 1. Springer.

GALLEE, H. & SCHAYES, G. 1994 Development of a 3-dimensional meso-γ primitive equation model: katabatic winds simulation in the area of Terra Nova Bay, Antarctica. *Mon. Weather Rev.* **122**, 671–685.

GILL, A. E. 1966 The boundary layer regime for convection in a rectangular cavity. *J. Fluid Mech.* **26**, 515–536.

GRISOGONO, B. & OERLEMANS, J. 2001 Analytic solution for gradually varying eddy diffusivities. *J. Atmos. Sci.* **58**, 3349–3354.

GRISOGONO, B. & OERLEMANS, J. 2002 Justifying the WKB approximation in pure katabatic flows. *Tellus* A **54**, 453–462.

Gutman, L. N. 1972 *Introduction to the Nonlinear Theory of Mesoscale Meteorological Processes* (Trans. from Russian). Israel Program for Scientific Translations, Jerusalem.

Gutman, L. N. 1983 On the theory of the katabatic slope wind. *Tellus* A **35**, 213–218.

Gutman, L. N. & Malbakhov, V. M. 1964 On the theory of katabatic winds of Antarctica. *Met. Issled.* 150–155.

Gutman, L. N. & Melgarejo, J. W. 1981 On the laws of geostrophic drag and heat transfer over a slightly inclined terrain. *J. Atmos. Sci.* **38**, 1714–1724.

Haiden, T. & Whiteman, C. D. 2005 Katabatic flow mechanisms on a low-angle slope. *J. Appl. Met.* **44**, 113–126.

Heinemann, G. & Klein, T. 2002 Modelling and observations of the katabatic flow dynamics over Greenland. *Tellus* A **54**, 542–554.

Helmis, C. G. & Papadopoulos, K. H. 1996 Some aspects of the variation with time of katabatic flow over a simple slope. *Q. J. R. Met. Soc.* **122**, 595–610.

Hunt, J. C. R., Fernando, H. J. S. & Princevac, M. 2003 Unsteady thermally driven flows on gentle slopes. *J. Atmos. Sci.* **60**, 2169–2182.

Imberger, J. & Patterson, J. C. 1990 Physical limnology. *Adv. Appl. Mech.* **27**, 303–475.

Klein, T., Heinemann, G., Bromwich, D. H., Cassano, J. J. & Hines, K. M. 2001 Mesoscale modeling of katabatic winds over Greenland and comparisons with AWS and aircraft data. *Met. Atmos. Phys.* **78**, 115–132.

Kondo, H. 1984 The difference of the slope wind between day and night. *J. Met. Soc. Japan* **62**, 224–233.

Lied, N. T. 1964 Stationary hydraulic jumps in a katabatic flow near Davis, Antarctica, 1961. *Austral. Met. Mag.* **47**, 40–51.

Lu, R. & Turco, R. P. 1994 Air pollutant transport in a coastal environment. Part I: Two-dimensional simulations of sea-breeze and mountain effects. *J. Atmos. Sci.* **51**, 2285–2308.

Lykosov, V. N. & Gutman, L. N. 1972 Turbulent boundary layer above a sloping underlying surface. *Izv. Acad. Sci. USSR, Atmos. Ocean. Phys.* **8**, 799–809.

Madsen, O. S. 1977 A realistic model of the wind-induced Ekman boundary layer. *J. Phys. Ocean.* **7**, 248–255.

Manins, P. C. & Sawford, B. L. 1979 A model of katabatic winds. *J. Atmos. Sci.* **36**, 619–630.

Monti, P., Fernando, H. J. S., Princevac, M., Chan W. C., Kowalewski, T. A. & Pardyjak, E. R. 2002 Observations of flow and turbulence in the nocturnal boundary layer over a slope. *J. Atmos. Sci.* **59**, 2513–2534.

Oerlemans, J. 1998 The atmospheric boundary layer over melting glaciers. *Clear and Cloudy Boundary Layers* (ed. A. A. M. Holtslag & P. G. Duynkerke), pp. 129–153. Royal Netherlands Academy of Arts and Sciences.

Papadopoulos, K. H., Helmis, C. G., Soilemes, A. T., Kalogiros, J., Papageorgas, P. G. & Asimakopoulos, D. N. 1997 The structure of katabatic flows down a simple slope. *Q. J. R. Met. Soc.* **123**, 1581–1601.

Parish, T. R. 1984 A numerical study of strong katabatic winds over Antarctica. *Mon. Weather Rev.* **112**, 545–554.

Parish, T. R. & Waight, K. T. 1987 The forcing of antarctic katabatic winds. *Mon. Weather Rev.* **115**, 2214–2226.

Peacock, T., Stocker, R. & Aristoff, M. 2004 An experimental investigation of the angular dependence of diffusion-driven flow. *Phys. Fluids* **16**, 3503–3505.

Pettré, P. & André, J.-C. 1991 Surface-pressure change through Loewe's phenomena and katabatic flow jumps: study of two cases in Adélie Land, Antarctica. *J. Atmos. Sci.* **48**, 557–571.

Phillips, O. M. 1970 On flows induced by diffusion in a stably stratified fluid. *Deep-Sea Res.* **17**, 435–443.

Prandtl, L. 1942 *Führer durch die Strömungslehre*. Vieweg, Braunschweig.

Renfrew, I. A. 2004 The dynamics of idealized katabatic flow over a moderate slope and ice shelf. *Q. J. R. Met. Soc.* **130**, 1023–1045.

Schlichting, H. 1979 *Boundary-Layer Theory*. McGraw-Hill.

Shapiro, A. 1996 Nonlinear shallow-water oscillations in a parabolic channel: exact solutions and trajectory analyses. *J. Fluid Mech.* **318**, 49–76.

SHAPIRO, A. 2001 A centrifugal wave solution of the Euler and Navier–Stokes equations. *Z. Angew. Math. Phys.* **52**, 913–923.

SHAPIRO, A. & FEDOROVICH, E. 2004 Unsteady convectively driven flow along a vertical plate immersed in a stably stratified fluid. *J. Fluid Mech.* **498**, 333–352.

SKYLLINGSTAD, E. D. 2003 Large-eddy simulation of katabatic flows. *Boundary-Layer Met.* **106**, 217–243.

STONE, G. L. & HOARD, D. E. 1989 Low-frequency velocity and temperature fluctuations in katabatic valley flows. *J. Appl. Met.* **28**, 477–488.

THACKER, W. C. 1981 Some exact solutions to the nonlinear shallow-water wave equations. *J. Fluid Mech.* **107**, 499–508.

TYSON, P. D. 1968 Velocity fluctuations in the mountain wind. *J. Atmos. Sci.* **25**, 381–384.

VERONIS, G. 1970 The analogy between rotating and stratified fluids. *Annu. Rev. Fluid Mech.* **2**, 37–66.

WUNSCH, C. 1970 On oceanic boundary mixing. *Deep-Sea Res.* **17**, 293–301.